# Wideband UHF DQPSK Backscatter Communication in Reverberant Cavity Animal Cage Environments

Apoorva Sharma, *Student Member, IEEE*, Eleftherios Kampianakis, *Student Member, IEEE*, James Rosenthal, *Student Member, IEEE*, Alexandra Pike, Anissa Dadkhah, *Student Member, IEEE*, and Matthew S. Reynolds, *Senior Member, IEEE*

***Abstract*— Many neuroscience experiments with animal subjects require free motion of the animal within a metal cage environment. In such cage environments, wireless communication with implanted devices, e.g., neural recording and stimulation is particularly challenging because the metal cage walls form a reverberant cavity with dense multipath. In the case of backscatter communication with the implanted device, the multipath challenge is particularly acute because of the round-trip nature of the backscatter channel. This paper demonstrates the reverberant cavity effect via measurement of the channel transfer function inside a metal cage used for nonhuman primate research in the 902–928 MHz ultrahigh-frequency industrial, scientific, and medical band. A reduced-size ceramic patch antenna developed for the Neurochip neural recording and stimulation device was affixed to a saline tissue proxy, while a commercial air-dielectric patch antenna was affixed to the ceiling of the cage. A measured 3 dB channel bandwidth greater than 6.5 MHz with a port-to-port insertion loss between 14 and 37 dB was achieved at 126 surveyed locations within the cage volume. A 6.25 Mb/s backscatter data uplink using a differential quadrature phase shift keying constellation was successfully validated inside the cage, with effectively 0% packet error rate for all but two of the surveyed locations. The simulation and experimental results show good agreement and reveal that wideband backscatter communication systems can perform well despite the significant multipath inside the reverberant cage environment.**

***Index Terms*— Backscatter communication, implanted biomedical devices, neural recording, reverberant cavity.**

## I. Introduction

THE advent of electrophysiological recording of single cortical neurons in awake monkeys [1] enabled new understanding of neuronal control of muscular movement. Building on these insights, neuroscientists have been able to relate neuronal firing rates to various movement parameters [2]–[5]. Traditionally, the relationship between neuron firing and physical behavior has been studied by artificially constraining the movement of a nonhuman primate (NHP) subject. Systematic control of the test environment reduces noise in neural recordings, enables precise measurement of the behavioral tasks, and prevents injury to the animal and damage to the wired equipment. However, stereotyped motion in these constrained experiments has been found to produce potentially misleading correlations between movement parameters [2]. To develop an unbiased understanding of the relationship between neural activity and movement, neural recording in free-moving animals is required.

The ability to accurately measure extracellular activity of individual neurons and neural ensembles has led to the development of neural prosthetics referred to as brain computer interfaces (BCIs). To enable fundamental neuroscience research in, e.g., induced neural plasticity in freely behaving animals, BCIs must be able to wirelessly stream neural recordings from multiple channels for multiple days in an unconstrained environment, such as the animal's home cage [6]–[9]. Conventional wireless standards such as Bluetooth Low Energy and Wi-Fi have undesirably high power consumption, which leads to poor battery life and the potential for tissue heating due to the combination of dc power dissipation

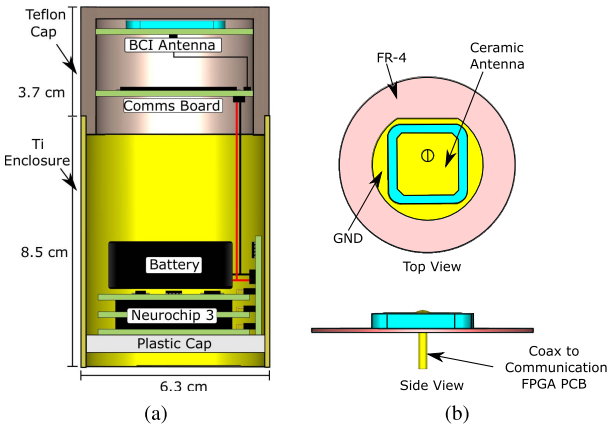


Fig. 1. Overview of the NC3 Assembly. (a) Stack up of the components inside the titanium (Ti) enclosure and the Teflon cap. (b) BCI Antenna configuration showing the ceramic patch, ground plane, FR-4 substrate, and the coax feed.

Manuscript received March 2, 2018; revised January 16, 2019; accepted January 17, 2019. Date of publication February 21, 2019; date of current version August 12, 2019. This work was supported in part by the National Science Foundation under Award EEC-1028725. *(Apoorva Sharma and Eleftherios Kampianakis are the co-first authors.) (Corresponding authors: Apoorva Sharma; Eleftherios Kampianakis.)*

A. Sharma, E. Kampianakis, J. Rosenthal, and A. Dadkhah are with the Department of Electrical Engineering, University of Washington, Seattle, WA 98195 USA (e-mail: mail2apoorva@gmail.com; kampianakis@gmail.com).

A. Pike is with Juanita High School, Kirkland, WA 98034 USA.

M. S. Reynolds is with the Department of Electrical Engineering, University of Washington, Seattle, WA 98195 USA, and also with the Paul G. Allen School of Computer Science and Engineering, University of Washington, Seattle, WA 98195 USA.

Color versions of one or more of the figures in this paper are available online at http://ieeexplore.ieee.org.

Digital Object Identifier 10.1109/TAP.2019.2900423

and high specific absorption rates (SARs) [10], [11]. Energy efficient, high-data-rate wireless data uplinks using backscatter could enable an external, nonpower-constrained computing device to analyze the recorded neural activity. For the case of bidirectional BCIs, such an external device could also determine an appropriate stimulation response using complex signal processing and/or machine learning approaches that are infeasible on a size- and power-constrained implanted device.

Unlike conventional radios, backscatter-based uplinks do not require power-hungry active RF amplifiers and oscillators to generate a communication carrier wave (CW). The CW is instead provided by an external transceiver having access to ample power. The backscatter-based device applies a time-varying impedance to its antenna, which modulates the amplitude and phase of the incident CW. The modulated signal is then scattered by the device's antenna. The backscatter modality allows for small-form factor systems with high data rates (>96 Mb/s) [12] at orders of magnitude less power consumption compared to Bluetooth Low Energy and Wi-Fi (IEEE 802.11n) [13]. Ultrawideband (UWB) [14] is a viable alternative to backscatter communication, but we feel that backscatter communication is an attractive choice for BCIs (from our perspective) due to its simplicity and lower power consumption compared with UWB and other alternatives.

The key tradeoff with backscatter is a less favorable link budget than conventional radios, because the communication CW must travel a round-trip path from the external system to the backscatter device and back to the external system. As a result, in free space, the received signal power is proportional to the inverse fourth power of distance [15]. This becomes problematic in locations with dense multipath fading, such as metal cages, where the metal walls form a reverberating cavity in which electromagnetic (EM) waves bounce back and forth. This phenomenon results in many deep nulls in the communication channel, which impair the backscattered signal. To design robust backscatter-based devices for BCI applications in freely moving NHPs, it is, therefore, necessary to understand the channel transfer function within the animal's home cage.

While there is extensive literature on characterizing multipath channels in urban and indoor office environments, to the best of our knowledge, this is the first characterization of the channel transfer function for the 902–928 MHz ultrahigh frequency (UHF) industrial, scientific, and medical (ISM) band inside of a metal primate cage. Furthermore, we demonstrate that backscatter communication systems can perform well inside of a metal primate cage despite the significant multipath inside the reverberant cage environment. We present EM simulation and test results of a 923 MHz ISM band wireless differential quadrature phase-shift keying (DQPSK) backscatter data uplink system designed for the Neurochip 3 (NC3) BCI system, the successor to the Neurochip 2 system [6], operating within an NHP cage. Moreover, we developed a comms board for the NC3, which provides real-time wireless backscatter data transfer capabilities. Together, the comms board, the antenna, a 13 Wh battery pack, and the NC3 compose the assembly (hereby referred to as the NC3 assembly) that is depicted in Fig. 1(a). The NC3 assembly is designed

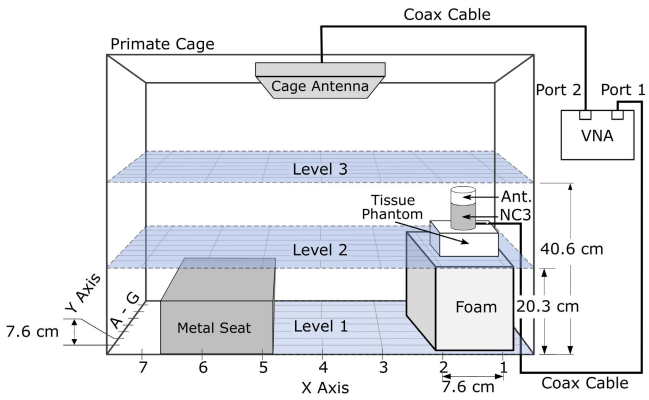


(a)

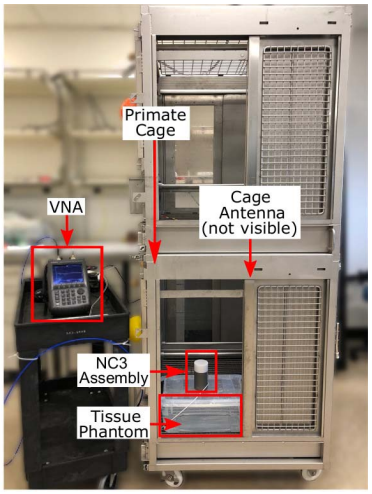


(b)

Fig. 2. (a) Block diagram and (b) photograph of the test setup used to characterize the wireless channel of the NHP cage.

to fit inside a titanium (Ti) tube, sealed with a Teflon cap, and fabricated to be mounted on the top of the skull of an NHP.

Section II presents the EM analysis and antenna design used for the system. Methods and results are presented for both the simulations and experiments performed inside the NHP cage using a saline tissue proxy to represent the NHP. Section III presents the architecture and design of the communication system, as well as testing of the system within the cage. Section IV provides conclusions from the results and a discussion of potential future work.

## II. Antenna Design and EM Analysis

In this paper, simulation and validation environments were arranged to mimic BCI experiments in a typical NHP cage similar to the one depicted in Fig. 2. Within the cage, two antennas were used in a monostatic backscatter configuration: a cage antenna affixed to the top wall of the lower chamber and a BCI antenna integrated into the NC3 assembly placed on the top of a tissue proxy or phantom consisting of a plastic container filled with tissue equivalent saline water.

A commercial antenna was chosen for the external (cage-mounted) side, whereas a semicustom BCI antenna was designed to fit inside the NC3 assembly's Teflon cap using a

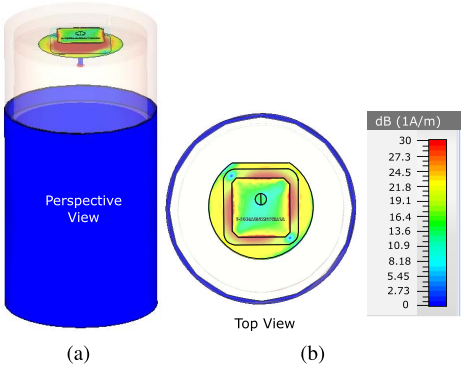


Fig. 3. Simulated frequency-domain surface current at 923 MHz showing maximum surface current along the patch antenna and minimum around the Ti enclosure.

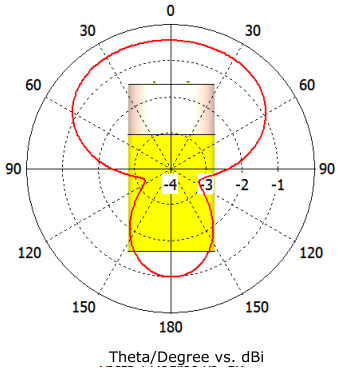


Fig. 4. Simulated gain pattern at 923 MHz showing a realized gain of −0.4 dBi on boresight.

commercial ceramic patch element. The NC3 electronics are contained in an 8.5 cm long, 6.3 cm outer diameter Ti tube. The Ti tube has an inner diameter of 6.1 cm, whereas the Teflon cap has an inner diameter of 5.6 cm, an outer diameter of 6.3 cm, and a length of 3.7 cm.

### A. Antenna Design

*1) Cage Antenna:* The cage antenna used in the experiments was a Laird Technologies S9028PCR right-hand circularly polarized, air-dielectric patch antenna whose −10 dB bandwidth is 902–928 MHz. The reported antenna gain is 8 dBic with a 70° beamwidth, and its overall dimensions with its plastic casing are 25.8 cm × 25.8 cm × 3.2 cm (length×width×height). Since freely moving animals may stand in any orientation relative to the cage antenna, a circularly polarized antenna was chosen to reduce signal losses from polarization mismatch.

*2) BCI Antenna:* The BCI antenna PCB shown in Fig. 1(b) is a two-layer board designed on a 1.6 mm thick FR-4 substrate with an outer diameter of 5.5 cm. The copper thickness is 30 $\mu$m. The top side of the BCI antenna PCB contains a centered, circularly shaped ground plane of 1.5 cm radius, which is bonded to the ground plane of an Abracon APAE915R2540ABDB1-T ceramic patch antenna. The antenna dimensions are 2.5 cm × 2.5 cm × 0.4 cm (length × width × height). The bottom side of the PCB is utilized to connect a balun and a ultra-miniature connector coaxial connector. The ceramic patch architecture was chosen because of the good tradeoff between its size and realized gain.

### B. Simulation Results

The performance of the BCI antenna was evaluated using the finite-element method solver built into CST Microwave Studio [16]. The simulations were performed with the BCI antenna PCB placed within the Teflon cap and connected to the Ti enclosure, similar to the experimental setup. Fig. 3 shows the frequency-domain simulation results of the surface currents flowing through the antenna and the Ti enclosure. It can be observed that the surface current is confined between the patch's top and bottom surfaces; much less current flows on the Ti enclosure. The simulation also suggests that the −10 dB bandwidth of the antenna is approximately 1 MHz centered at 923 MHz. The maximum realized gain of the antenna is −0.4 dBi at the center frequency of 923 MHz (Fig. 4).

### C. Experimental Setup

The NHP cage depicted in Fig. 1 was utilized for the experiments. The cage is divided into two chambers (top and bottom) by a horizontal metal grating. Measurements were conducted in the lower chamber of the cage with dimensions of 93 cm × 93.4 cm × 77 cm (height ×width × length). All the walls of the cage are made with a square metal mesh with a mean gap of 2.5 cm. This gap is ten times smaller than the shortest wavelength of 32.3 cm in the UHF band, and therefore, it can be viewed as an impenetrable metal wall for in-band signals. However, the cage is not a perfectly enclosed EM cavity, because one of the vertical walls of the cage contains a clear polycarbonate window with dimensions of 60.7 cm × 23.4 cm (length × width), through which EM waves may propagate. Finally, the cage contains a metal seat for the NHPs with a width of 18 cm and a height of 15 cm.

A saline tissue phantom was used to simulate the body of a male macaque monkey weighing 7 kg on average; this species is frequently used in neural plasticity experiments [2]. The phantom consists of a plastic container with dimensions of 41.8 cm × 27.8 cm × 16.5 cm (length × width × hfeight) and contains 7 L of saline solution with 0.91 g sodium chloride (NaCl) per liter of distilled water [17]. The NC3 assembly was placed on the top of the plastic container. The BCI antenna was connected to port 1 of a Keysight FieldFox vector network analyzer (VNA) with a coaxial cable, and the cage antenna was connected to port 2 of the VNA with another coaxial cable. We performed a two-port calibration of the coaxial cables and VNA prior to measurement. To further mitigate cable effects, we routed the cables away from the direct path between the antennas and perpendicular to the antenna plane as much as possible, routing the cable along the metal cage walls.

The antenna performance was measured at multiple locations within the cage. As shown in Fig. 2(a), we divided the cage's interior volume into three horizontal levels, labeled 1–3 from bottom to top, with a vertical spacing between Levels

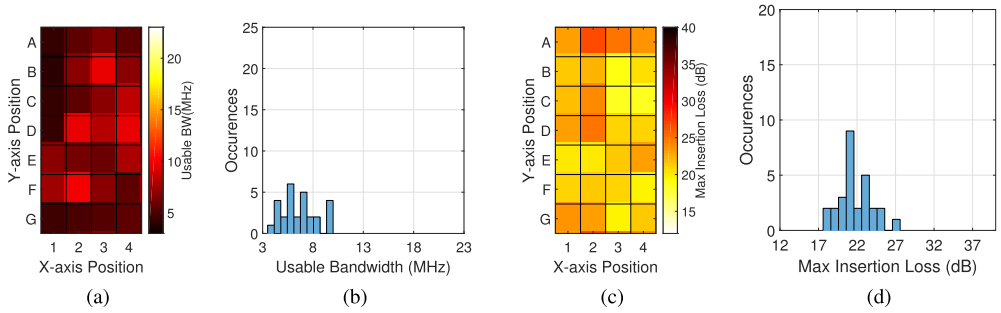


Fig. 5. Experimental results at Level 1 showing (a) heatmap and (b) histogram of usable bandwidth, and (c) heatmap and (d) histogram of maximum insertion loss. In all heatmap images, darker colors indicate worse performance.

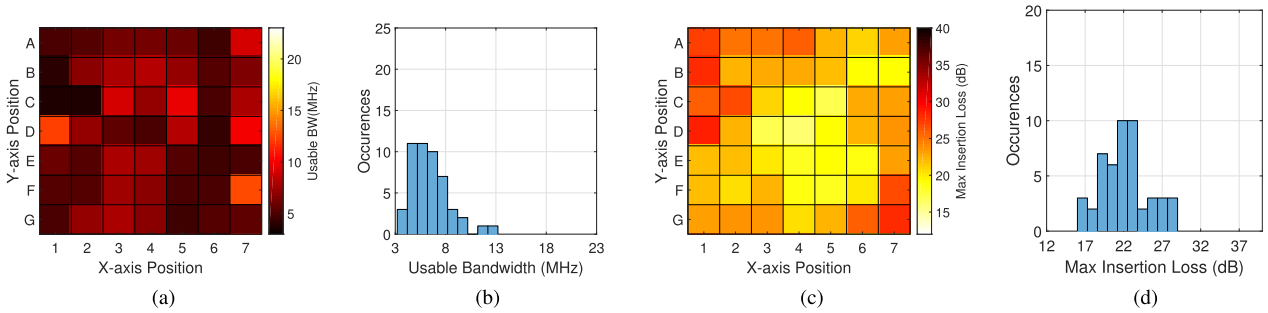


Fig. 6. Experimental results at Level 2 showing (a) heatmap and (b) histogram of usable bandwidth, and (c) heatmap and (d) histogram of maximum insertion loss. In all heatmap images, darker colors indicate worse performance.

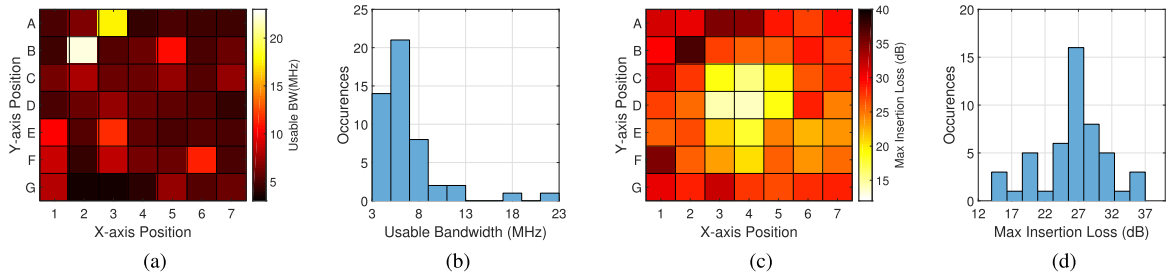


Fig. 7. Experimental results at Level 3 showing (a) heatmap and (b) histogram of usable bandwidth, and (c) heatmap and (d) histogram of maximum insertion loss. In all heatmap images, darker colors indicate worse performance.

of 20.3 cm. An RF-transparent Styrofoam block was utilized to raise the tissue phantom height to Levels 2 and 3. These levels were, in turn, subdivided into a 7.6 cm $\times$ 7.6 cm square grid. All measurement positions were conducted in the center of these squares. The edges of each space were labeled from 1 to 7 and from A to G for the $x$-axis and the $y$-axis, respectively. Thus, the center of the cage corresponds to location D4. Levels 2 and 3 contain 49 measurement locations. However, for Level 1, the experiments were performed from rows A to G along the $y$-axis but only from columns 1 to 4 along the $x$-axis, due to the placement of the metal seat, giving a total of 28 measurement locations.

### *D. Experimental Results*

The BCI antenna performance was characterized in terms of its 3 dB bandwidth (in megahertz), insertion loss (in decibels), and orientation sensitivity. The bandwidth and the insertion loss were measured at each different measurement location for all three levels. Figs. 5–7 depict the aggregated results where darker colors indicate smaller bandwidth or higher insertion loss. The mean 3 dB bandwidth (which we considered to be the "Usable" bandwidth) was found to be 6.56, 6.50, and 6.70 MHz for Levels 1, 2, and 3, respectively. The maximum insertion loss inside the 3 dB bandwidth was measured at 27.6 dB, 28.7 dB, and 37 dB for Levels 1, 2 and 3, respectively. It is important to note that, due to the cavity effects, the 3 dB bandwidth across all 126 measurement location varies from 3.4 to 22 MHz, and the best case insertion loss and the worst case insertion loss are 14 dB and 37 dB, respectively.

The insertion loss was found to be generally smaller at the center of the cage and higher at the edges of the cage due to multiple reflections from the edges. As shown in Fig. 8, the reflection coefficient $S_{11}$ (in decibels) of the BCI antenna is better than $-10$ dB across the 921.5–924 MHz band (2.5 MHz BW), while in seven of the nine test locations, the $-10$ dB bandwidth was around 921.5–928 MHz (6.5 MHz BW).

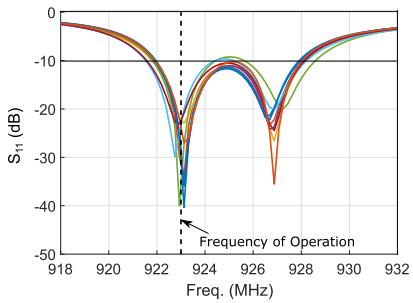


Fig. 8. Measured $S_{11}$ (in decibels) of the BCI antenna at nine different locations. In two of the nine locations, the −10 dB bandwidth was ≈921.5–924 MHz, and for the remaining seven locations, the −10 dB bandwidth was ≈921.5–928 MHz.

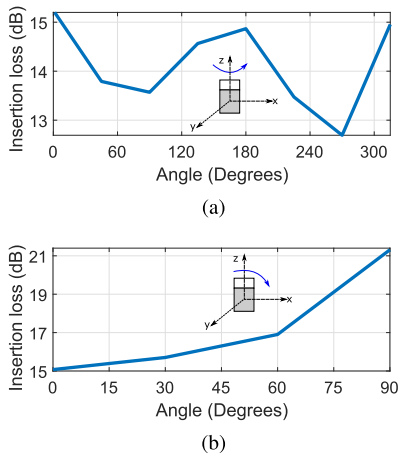


Fig. 9. Measured insertion loss at 923 MHz. (a) Rotation along $z$-axis. (b) Elevation angle from $z$-axis to $x$-axis.

We also characterized the orientation sensitivity of the BCI antenna relative to the cage antenna. The saline phantom and the NC3 assembly were placed in the center of Level 2 (location D4) and rotated along their vertical $Z$-axis with a step of 45° ranging from 0° to 330° and along an elevation angle with a step of 30°, ranging from 0° to 90°. The results are depicted in Fig. 9, showing a maximum orientation impairment of 2.55 dB along the vertical Z-axis and a maximum orientation impairment of 6.24 dB along the elevation angle.

### *E. SAR Simulation*

Tissue heating induced by EM radiation is commonly described by the SAR measured in Watts per kilogram (W/kg) as can be calculated by the following equation:

$$\mathrm{SAR} = \frac{1}{V}\int \frac{\gamma \times |E(r)|^2}{\rho}\mathrm{d}r, \tag{1}$$

where $\gamma$ is the electrical conductivity, $E$ is the rms electric field, $r$ is a position vector, $\rho$ is the density of the sample, and $V$ is the volume of the sample.

The time-domain solver module built into CST was employed to estimate the SAR on the tissue phantom. In the simulation setup, the cage antenna was driven with a continuous wave at 923 MHz with a power of 1 W (30 dBm). The peak SAR for the saline phantom was simulated for locations D1, D4, and D7 at Level 2. The dielectric properties of saline were calculated using the Debye first-order model at room temperature [18]. To our knowledge, there is no established SAR measurement procedure for NHPs nor established limits. The SAR in a saline solution model can be considered as worst case due to the higher conductivity of the saline versus NHP tissue [19]. As shown in Fig. 10, the maximum calculated value that was obtained is 0.6 W/kg averaged over 1 g of saline mass. This is well below the regulatory limit of 1.6 W/kg for human exposure that is imposed by the Federal Communications Commission (FCC) in the United States. We expect the actual SAR to be ≈20 dB smaller than the simulated values, because for the actual experiments, a 10 dBm peak transmit power was utilized.

### *F. Discussion and System Design Implications*

The experimental results shown in Figs. 5–7 clearly illustrate the dense multipath present inside the reverberant cavity environment of the metal animal cage. It is clear from these measurements that a system design assuming free-space propagation is doomed to be unreliable in the cage environment due to the deep nulls occurring only a few centimeters apart. In this paper, we took a conservative approach to the backscatter uplink design, by selecting a symbol rate of 3.125 MHz, which would essentially always be supported by the available channel bandwidth. On the basis of these experiments, we suggest that more complex future systems incorporating real-time channel equalization could achieve greater capacity but at the expense of design complexity and increased dc power consumption.

From the perspective of NHP animal safety, the simulated SAR values indicate that a carrier power of 10 dBm would always be safe for continuous exposure of the NHP animal subject, with a safety factor of more than 20 dB. Carrier power of up to 30 dBm could potentially be safe for the NHP subject, but more detailed simulation would be required to justify that premise. For our purposes, the 10 dBm carrier power level was sufficient to achieve the communication link quality goal and is comfortably within safe limits for human exposure.

## III. Communication System Design

The existing NC3 brain–computer interface device employs an Intan RHD2132 integrated circuit (IC) to amplify and digitize the neural data and a field-programmable gate-array (FPGA)-driven flash memory for recording. In the existing NC3 system, the data are extracted postexperiment using an infrared data link that can operate at a maximum range of only a few centimeters. In order to telemeter the neural signals from the NC3 in real time, over the entire NHP cage area, we developed the following DQPSK backscatter-based data uplink system.

The system design is depicted in Fig. 11. A PC connected to a software-defined radio (SDR) generates a UHF CW carrier that is amplified and transmitted inside the NHP cage via the cage antenna. The CW carrier is backscattered from the BCI antenna described above in Section II and connected to an FPGA-based communications board (hereby referred to as the "comms board"). The backscattered signals are received by the

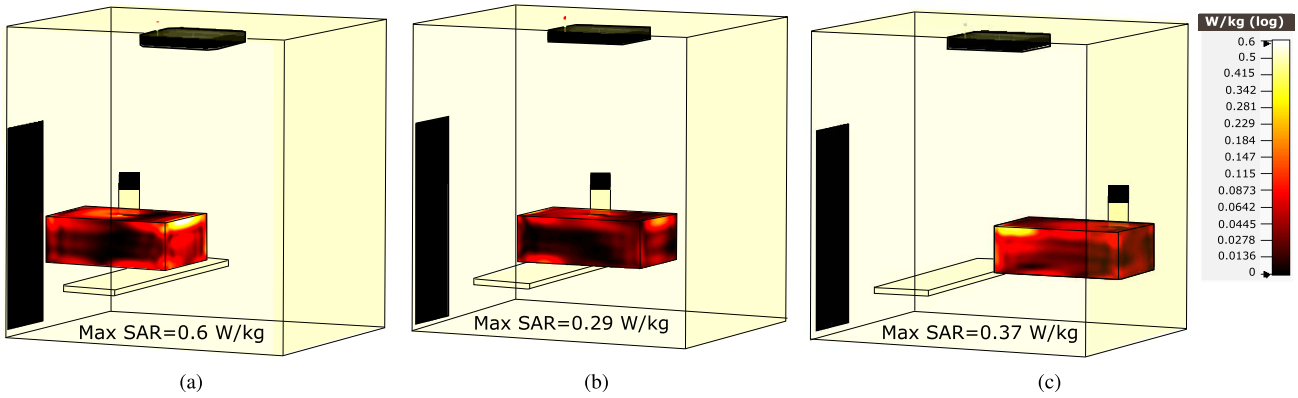


Fig. 10. Simulated SAR for the input power of 1 W (30 dBm) transmitted from the cage antenna. The peak SAR value obtained from all three positions is well below the FCC regulatory limit of 1.6 W/kg for human exposure.

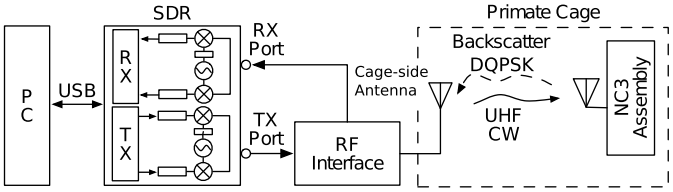


Fig. 11. Backscatter data uplink block diagram.

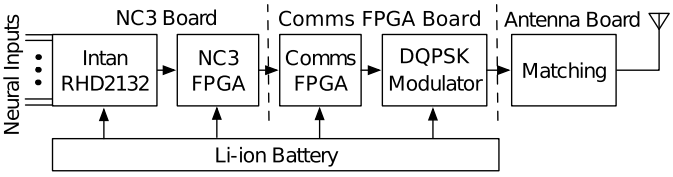


Fig. 12. NC3 + backscatter comms board assembly block diagram.

SDR and demodulated in real time via a combination of GNU Radio and MATLAB code. An RF interface block performs the carrier amplification and self-jammer canceling functions needed for the backscatter link. Section III-A–D describes these components in detail.

### *A. NC3 Assembly Design*

As shown in Fig. 12, the data generated by the Intan IC are collected by the on-board FPGA of the NC3 and sent to an Altera MAX 10 FPGA on the comms board using serial peripheral interface. There, the data are packetized and encoded with a Hamming (16, 11) code (15 bits plus 1 parity bit). The resulting packets are transmitted using DQPSK backscatter modulation and include data from 16 channels of the NC3 at a rate of 5 KHz. The packets are 1024 bits long and consist of 64 words of 16 bits length including the payload that includes a Barker code for start-of-frame (SOF) synchronization, the device ID, and a packet counter. This board consumes 198 mW at 3.3 V mainly due to the relatively large and power-hungry FPGA.

### *B. DQPSK Backscatter Modulation*

For this paper, we selected a DQPSK backscatter modulation that is implemented using an Analog Devices ADG904 RF

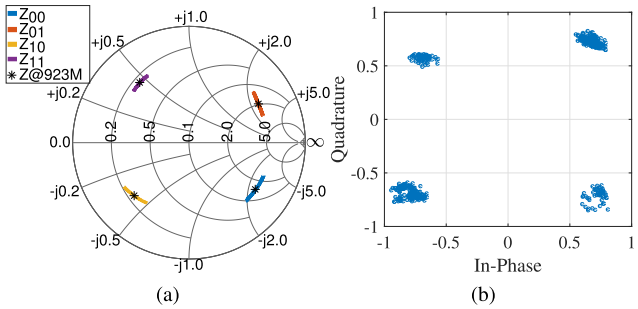


Fig. 13. (a) S11 measurements of the DQPSK backscatter modulator for four different impedance states. (b) Symbol constellation recorded over 5000 symbol periods.

single-pole-quadruple-throw switch, connected to 4 carefully chosen impedances that yield the four symbol states as described in [20]. The DQPSK modulation was employed because it can be implemented with small-form factor components that consume less than 10 $\mu$W and is twice as spectrally efficient than a typical binary modulation. The differential symbols facilitate the demodulation process by eliminating the phase ambiguity created by device movement within the reverberant cavity environment.

Fig. 13(a) depicts the measured $S_{11}$ values across the UHF ISM band, looking into the RF switch using a calibrated VNA. One can observe that the reflection coefficients for the four different switch states form a constellation on the Smith chart, corresponding to the four different symbol phases of the quadrature phase-shift keying (QPSK) signal [20].

To measure the error vector magnitude (EVM) of the backscatter modulator, we collected 5000 symbols using the receiver pipeline inside the NHP cage, in position D4, Level 1. The symbols, which are depicted in Fig. 13(b), were compared to an ideal QPSK constellation and an EVM of 9.7% was calculated. The resulting EVM is primarily due to the tolerances of the passive components installed on the backscatter modulator.

### *C. Software-Defined Radio Receiver*

To receive the incoming backscattered DQPSK signals, we expand the capabilities of the receiver that we developed

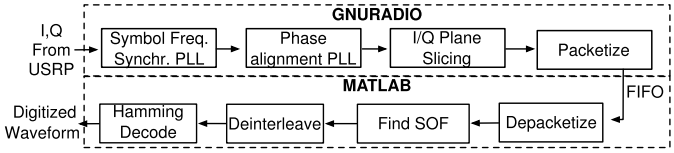


Fig. 14. Receiver pipeline. GNUradio and MATLAB scripts are responsible for demodulating the incoming I/Q data from the USRP.

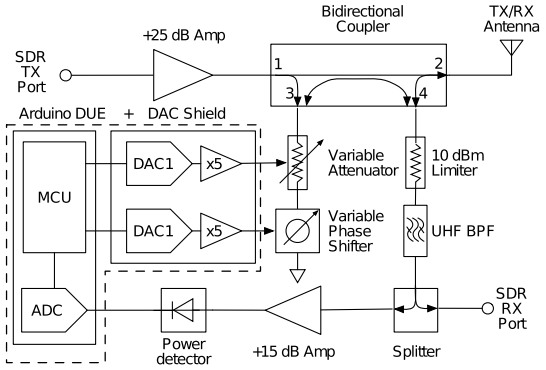


Fig. 15. Block diagram of the RF interface.

in [21] to accommodate the higher order modulation (DQPSK instead of binary phase shift keying).

The hardware components of the receiver include the Ettus universal software radio peripheral (USRP) B210, a low-cost ($1100) SDR. The USRP is used to generate the CW carrier at 923 MHz that is backscattered by the NC3 assembly. The USRP downconverts the backscattered signal to in-phase/quadrature (I/Q) baseband and samples the baseband at a rate of up to 50 MSamples/s. The sampled I/Q symbols are sent to an Intel Core i7 PC having a 3.8 GHz clock rate and 16 GB of memory. This PC supports processing of 200 packets at a time in real time using GNUradio and MATLAB software.

Fig. 14 depicts the receiver pipeline. A GNUradio flowgraph implements symbol frequency synchronization, phase alignment, and slicing of the incoming I/Q symbols from the USRP. The resulting data are transferred to a MATLAB script using a Linux pipe, where SOF synchronization is conducted, using the Barker codes that are embedded in the backscattered packets. Finally, deinterleaving and Hamming decoding are performed to extract the corresponding neural data stream, and the resulting waveform is plotted and saved to disk for further analysis.

### *D. RF Interface and Self-Jammer Cancelation*

One of the challenges of backscatter communication systems is the reception and demodulation of the backscattered signals in the presence of a CW (a self-jammer) that is typically much stronger [22]. To address this challenge, numerous approaches to isolate the transmit and receive paths have previously been explored [23]–[25]. We determined, based on the experimental results presented above, that the reverberant cavity environment of the NHP cage makes a self-jammer cancelation system essential to achieve good performance on a backscatter uplink.

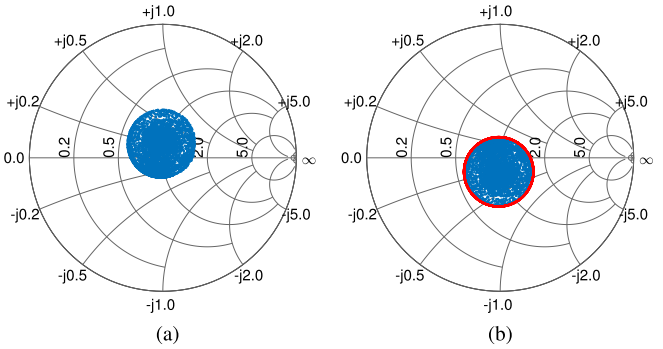


Fig. 16. (a) VNA measurement of 6500 out of the possible ≈16 million states of the variable reflective load. (b) Achievable self-jammer cancelation states. The red ring designates the boundary of this area.

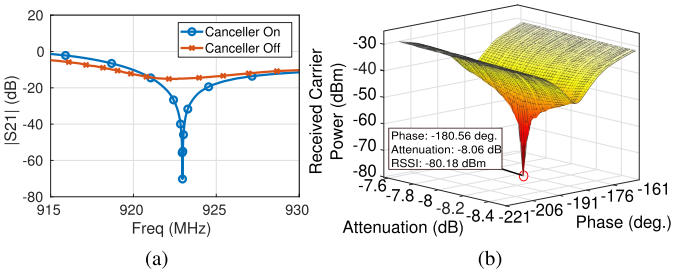


Fig. 17. (a) Measured insertion loss between the input- and output-coupled ports of the coupler. (b) Measured received self-jammer carrier power as a function of phase and attenuation of the reflection load.

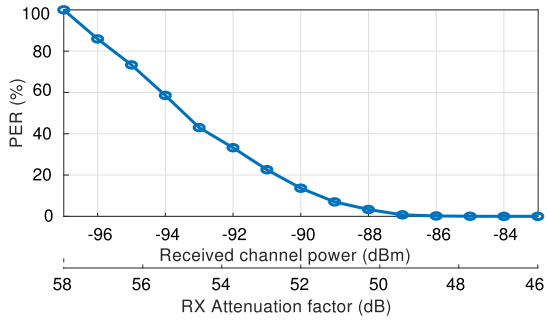


Fig. 18. PER versus absolute received channel power and receive path attenuation. The receiver exhibits a PER of less than 0.2% at an input backscatter power of −86 dBm.

In this paper, we develop an RF interface that can amplify the CW carrier by 25 dB and, most importantly, provide self-jammer cancelation of up to 95 dB. Self-jammer cancelation is extremely important for the receiver due to the poor 1 dB compression point performance of the low-noise amplifiers installed on the receive ports of the USRP. This effect can occur on the USRP at a received carrier power of as low as −70 dBm at the maximum receive gain setting. That is not surprising since the USRP is a multipurpose device and is not specifically designed for backscatter communication.

A block diagram of the RF interface is depicted in Fig. 15. This interface implements self-jammer cancelation by terminating the input-coupled port of a bidirectional coupler with a variable reflection coefficient. A variable reflection coefficient was implemented with a phase shifter and an attenuator connected in series and terminated with a short circuit.

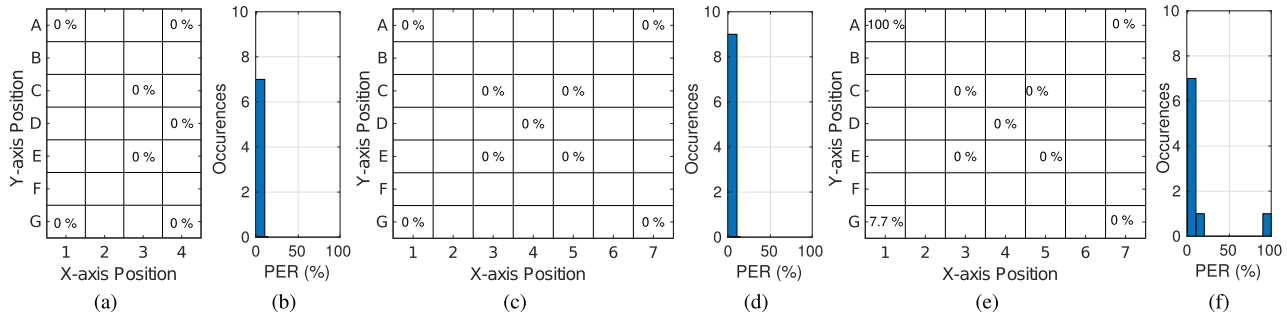


Fig. 19. PER measurements for different locations inside the NHP cage. (a)–(d) Measurements for Levels 1 and 2 indicate a PER of 0%. (e) and (f) Measurements at Level 3 demonstrate that the deep nulls affect the receiver's performance, as expected.

When the impedance at port 3 of the coupler is the conjugate of the cage antenna impedance, maximum isolation is achieved [23]. In our case, the received carrier power is measured using a sensitive power detector.

As shown in Fig. 15, our implementation employs a voltage-variable phase shifter with 0–360° range connected in series with a voltage-variable attenuator with 3–40 dB attenuation range and terminated with a short-circuit. The control voltages for both devices are generated by two digital-to-analog converters (DACs) with a resolution of 12 bits. The DACs are controlled by an Arduino Due platform through $I^2C$ and amplified with a gain of 5× resulting in a control voltage range of 0.7–15 V. The theoretical phase and attenuation resolution using the 12 bit DACs is calculated to be 0.08° and 0.006 dB, far exceeding the practical control requirement. High resolution is critical for the circuit performance since it enables tracking of the narrow-band phase/attenuation notch that achieves the optimal isolation results.

Fig. 16(a) depicts 6500 out of the over 16 million possible impedance states, and Fig. 16(b) depicts the corresponding cage antenna impedance values that the circuit can be used to cancel. The size of the occupied area is dependent on the total insertion loss of the variable reflection coefficient circuit, which was measured at 8 dB. However, the cage antenna that was utilized in this paper has a typical return loss of 17 dB, so the available load impedance states are sufficient for precise tuning.

Fine-tuning of the variable reflection coefficient circuit to match the impedance of the cage antenna involves a search [23] over a limited range of phase-attenuation pairs, to minimize the received signal power. In our implementation, a two-pass approach is used, where a quick search with coarse resolution determines the phase and attenuation ranges. A second, more refined search over the discovered range is used to fine-tune to the optimal setting. This algorithm is executed by the Arduino Due board and allows for the two-pass search to be completed in less than 2 seconds. Finally, a faster and more dynamic tuning is possible by continuously executing the search over a small moving window of phase/attenuation pairs.

### *E. Experimental Results*

The receiver setup was tested both in a bench-top environment and in the NHP cage that is depicted in Fig. 1. The results that are presented in this section validate that the system can be used for future *in vivo* collection of neural data on an NHP.

*1) Isolation Circuit Characterization:* Using a VNA, we measured the S-parameters between the output-coupled port and the input of the directional coupler looking into the CW amplifier. The NC3 assembly was placed at a distance of 40 cm from the cage antenna inside the NHP cage. Subsequently, we tuned the isolation circuit for a carrier frequency of 923 MHz and measured the insertion loss over the range of 915–930 MHz. We also took the same measurement using an untuned 50 Ω load connected in the place of the variable load for comparison. The results are presented in Fig. 17(a) where an insertion loss of up to 65 dB can be observed, representing an improvement of 55 dB compared to the untuned case.

We also measured the received self-jammer power as a function of the phase and attenuation of the reflective load in the NHP cage. With a carrier power of 15 dBm, Fig. 17(b) depicts the corresponding results where a deep and sharp null of −80 dBm can be observed at a phase and attenuation of −180.56° and −8.06 dB, respectively. This amounts to a self-jammer cancelation (transmit minus received power) of 95 dB, which validates the benchtop measurement and allows for the use of the full receive gain range of the USRP.

*2) DQPSK Receiver Chain Characterization:* To characterize the receiver sensitivity, we used a connectorized setup, introducing a variable attenuator to reduce the channel power available to the receiver in 1 dB steps from 46 to 58 dB of attenuation. This corresponds to an absolute channel power range of −83 to −96 dBm. As shown in Fig. 18, the receiver system exhibits a packet error rate (PER) of less than 0.2% at an input backscatter channel power of −86 dBm and a PER of 100% at an input backscatter power of −97 dBm.

*3) Link Budget Characterization:* The round-trip link budget for this system can be summarized as follows:

$$P_R = P_C + 2 \times S_{21} + M - S_{\text{cp}} \tag{2}$$

where $P_R$ is the received power at the cage-side antenna in dBm, $M$ is a modulation factor imposed by the symbol-dependent change in modulator impedance as seen by the NC3 antenna (akin to the free-space differential radar cross section), $S_{\text{cp}}$ denotes the losses involved in the RF interface due to the coupler and cabling, and $P_C$ denotes the CW power from the cage antenna. In our case, we used the two impedances that correspond to the smallest symbol

distance and calculated $M = -23.9$ dB. The measured losses of the RF interface indicate an $S_{cp} = 12$ dB. Based on these calculations and the measured sensitivity of the receiver system, any insertion loss higher than 30 dB will result in a 100% PER.

*4) PER Measurements in the NHP Cage:* Finally, we conducted PER measurements inside the NHP cage to evaluate the end-to-end performance of the system throughout the entire cage volume. For this wireless setup, the USRP was programed to output a 923 MHz carrier yielding a power of $P_C = 10$ dBm at the output of the coupler. Subsequently, a total of $10^4$ packets were collected for each position after the automated self-jammer cancelation tuning completed. Fig. 19 depicts the collected data. It can be observed that a reliable link can be established in all but one corner location (Level 3, position A1). The high PER at this position is due to a deep null in the channel with an insertion loss of 33 dB, as shown in Fig. 7. As expected from the return link budget, the link margin is inadequate in this location. To mitigate the adverse effect of the deep nulls, the transmit power could be adaptively increased when a nonzero PER is detected, or the data rate could be adaptively varied to accommodate reduced signal-to-noise ratio.

## IV. Conclusion

This paper presents a DQPSK backscatter-based UHF wireless data uplink system for a BCI device to be used with NHP subjects. The goal of this paper is to enable real-time data uplink from neuroscience experiments in freely behaving animals. The reverberant cavity EM environment of the NHP cage was modeled using full-wave simulation software and measured data are presented. Measurements with a saline tissue proxy at 126 surveyed locations inside an actual NHP cage indicated a typical 3 dB bandwidth of 6.56 MHz and an insertion loss of 27.6–37 dB.

Based on these measurements, a UHF-band, DQPSK monostatic backscatter data uplink was successfully designed and validated inside the cage, exhibiting 0% PER for all but two of the measurement locations at a symbol rate of 3.125 MHz (i.e., a bit rate of 6.25 Mb/s). This result demonstrates that, even in the harsh reverberant cavity environment of an NHP animal cage, a wideband backscatter uplink is a practical choice for data uplink from BCI systems.

Our measurements suggest that, with channel equalization, a more complex backscatter data uplink system could yield much higher data rates, albeit at an increase in system power consumption and complexity. The future work with this system includes *in vivo* testing of the complete setup with NHP subjects in order to evaluate the system in the intended neuroscience research context.

## Acknowledgment

The content is solely the responsibility of the authors and does not necessarily represent the official views of the National Science Foundation.

The authors would also like to thank Prof. E. E. Fetz, Prof. S. I. Perlmutter, Prof. A. Yazdan-Shahmorad, and the team at the Washington National Primate Research Center for providing sample neural recordings and access to the NHP cage.

## References

[1] E. V. Evarts, "Temporal patterns of discharge of pyramidal tract neurons during sleep and waking in the monkey," *J. Neurophysiol.*, vol. 27, no. 2, pp. 152–171, Mar. 1964.

[2] A. Jackson, J. Mavoori, and E. E. Fetz, "Correlations between the same motor cortex cells and arm muscles during a trained task, free behavior, and natural sleep in the macaque monkey," *J. Neurophysiol.*, vol. 97, no. 1, pp. 360–374, Jan. 2007.

[3] A. P. Georgopoulos, J. F. Kalaska, R. Caminiti, and J. T. Massey, "On the relations between the direction of two-dimensional arm movements and cell discharge in primate motor cortex," *J. NeuroSci.*, vol. 2, no. 11, pp. 1527–1537, 1982.

[4] P. D. Cheney and E. E. Fetz, "Functional classes of primate corticomotoneuronal cells and their relation to active force," *J. Neurophysiol.*, vol. 44, no. 4, pp. 773–791, 1980.

[5] T. N. Aflalo and M. S. A. Graziano, "Partial tuning of motor cortex neurons to final posture in a free-moving paradigm," *Proc. Nat. Acad. Sci. USA*, vol. 103, no. 8, pp. 2909–2914, Feb. 2006.

[6] S. Zanos, A. G. Richardson, L. Shupe, F. P. Miles, and E. E. Fetz, "The Neurochip-2: An autonomous head-fixed computer for recording and stimulating in freely behaving monkeys," *IEEE Trans. Neural Syst. Rehabil. Eng.*, vol. 19, no. 4, pp. 427–435, Aug. 2011.

[7] X. Liu, M. Zhang, A. G. Richardson, T. H. Lucas, and J. Van der Spiegel, "Design of a closed-loop, bidirectional brain machine interface system with energy efficient neural feature extraction and PID control," *IEEE Trans. Biomed. Circuits Syst.*, vol. 11, no. 4, pp. 729–742, Aug. 2017.

[8] M. Yin, D. A. Borton, J. Aceros, W. R. Patterson, and A. V. Nurmikko, "A 100-channel hermetically sealed implantable device for chronic wireless neurosensing applications," *IEEE Trans. Biomed. Circuits Syst.*, vol. 7, no. 2, pp. 115–128, Apr. 2013.

[9] T. Libey and E. E. Fetz, "Open-source, low cost, free-behavior monitoring, and reward system for neuroscience research in non-human primates," *Frontiers Neurosci.*, vol. 11, p. 265, May 2017.

[10] H. P. Jammet *et al.*, "Guidelines on limits of exposure to radiofrequency electromagnetic fields in the frequency range from 100 kHz to 300 GHz, " *Int. Commission Non-Ionizing Radiat. Protection*, vol. 54, no. 1, pp. 115–123, 1988.

[11] P. J. Dimbylow and S. M. Mann, "SAR calculations in an anatomically realistic model of the head for mobile communication transceivers at 900 MHz and 1.8 GHz," *Phys. Med. Biol.*, vol. 39, no. 10, p. 1537, 1994.

[12] S. J. Thomas and M. S. Reynolds, "A 96 Mbit/sec, 15.5 pJ/bit 16-QAM modulator for UHF backscatter communication," in *Proc. IEEE Int. Conf. RFID*, Apr. 2012, pp. 185–190.

[13] J. F. Ensworth and M. S. Reynolds, "Every smart phone is a backscatter reader: Modulated backscatter compatibility with Bluetooth 4.0 low energy (BLE) devices," in *Proc.IEEE Int. Conf. RFID*, Apr. 2015, pp. 78–85.

[14] A. Ebrazeh and P. Mohseni, "30 pJ/b, 67 Mbps, centimeter-to-meter range data telemetry with an IR-UWB wireless link," *IEEE Trans. Biomed. Circuits Syst.*, vol. 9, no. 3, pp. 362–369, Jun. 2015.

[15] J. D. Griffin and G. D. Durgin, "Complete link budgets for backscatter-radio and RFID systems," *IEEE Antennas Propag. Mag.*, vol. 51, no. 2, pp. 11–25, Apr. 2009.

[16] CST. *Microwave Studio*. Accessed: Mar. 2, 2018. [Online]. Available: https://www.cst.com/products/cstmws

[17] A. Sharma, E. Kampianakis, and M. S. Reynolds, "A dual-band HF and UHF antenna system for implanted neural recording and stimulation devices," *IEEE Antennas Wireless Propag. Lett.*, vol. 16, pp. 493–496, 2017.

[18] A. Stogryn, "Equations for calculating the dielectric constant of saline water (correspondence)," *IEEE Trans. Microw. Theory Techn.*, vol. MTT-19, no. 8, pp. 733–736, Aug. 1971.

[19] J. S. Besnoff and M. S. Reynolds, "Single-wire RF transmission lines for implanted devices," in *Proc. IEEE Biomed. Circuits Syst. Conf. (BioCAS)*, Nov. 2013, pp. 222–225.

[20] S. J. Thomas, R. R. Harrison, A. Leonardo, and M. S. Reynolds, "A battery-free multichannel digital neural/EMG telemetry system for flying insects," *IEEE Trans. Biomed. Circuits Syst.*, vol. 6, no. 5, pp. 424–436, Oct. 2012.

[21] E. Kampianakis, A. Sharma, J. Arenas, and M. S. Reynolds, "A dual-band wireless power transfer and backscatter communication approach for real-time neural/EMG data acquisition," *IEEE J. Radio Freq. Identif.*, vol. 1, no. 1, pp. 100–107, Mar. 2017.
[22] D. M. Dobkin, *The RF in RFID: UHF RFID in Practice*. Boston, MA, USA: Elsevier, 2008.
[23] A. Boaventura, J. Santos, A. Oliveira, and N. B. Carvalho, "Perfect isolation: Dealing with self-jamming in passive RFID systems," *IEEE Microw. Mag.*, vol. 17, no. 11, pp. 20–39, Nov. 2016.
[24] J. Carrick, R. Herold, M. Reynolds, Y. Maguire, and R. Pappu, "Methods and apparatus for self-jamming suppression in a radio frequency identification (RFID) reader," U.S. Patent 0 069 011 A1, Mar. 18, 2010.
[25] M. Koller and R. Küng, "Adaptive carrier supression for UHF RFID using digitally tunable capacitors," in *Proc. Eur. Microw. Conf.*, Oct. 2013, pp. 943–946.

**Apoorva Sharma** (S'15) received the B.Tech. degree in electronics and communication engineering from the Galgotias College of Engineering and Technology, Greater Noida, India, in 2009, and the M.Sc.(Tech.) degree from the International Institute of Information Technology Hyderabad, Hyderabad, India, in 2011. She is currently pursuing the Ph.D. degree with the Department of Electrical Engineering, University of Washington, Seattle, WA, USA.

From 2011 to 2013, she was the Application Engineer with Computer Simulation Technology, Bangalore, India, where she was responsible for technical support and benchmarks for CST Microwave Studio, Cable Studio, Particle Studio, and Design Studio software. She was involved in improving the database of Antenna Magus. Her current research interests include modeling and optimization techniques of RF devices, electromagnetics, antenna designs, and implantable devices.

**Eleftherios Kampianakis** (S'15) received the B.S. and M.S. degrees in electronic and computer engineering from the Technical University of Crete, Chania, Greece. He is currently pursuing the Ph.D. degree with the Department of Electrical Engineering, University of Washington, Seattle, WA, USA. His diploma thesis was focused on over-the-air programmable wireless sensor networks (WSNs).

He developed a low-cost and low-power WSN for environmental sensing exploiting backscatter communication principles. His current research interests include backscatter communication and implantable biomedical devices.

Mr. Kampianakis was a recipient of the Best Diploma Thesis Award on the Pan-Hellenic IEEE VTS & AESS Joint Greece Chapter Final/Diploma Thesis Competition for the years 2009–2011. His contribution has been selected as one of the best papers at the IEEE SENSORS Conference 2013.

**James Rosenthal** (S'16) received the B.S. degree in electrical engineering from the University of Minnesota, Minneapolis, MN, USA, in 2013, and the M.S. degree in electrical engineering from the University of Washington, Seattle, WA, USA, in 2018, where he is currently pursuing the Ph.D. degree with the Department of Electrical and Computer Engineering.

From 2013 to 2016, he was an Electrical Engineer with the NASA Langley Research Center, Hampton, VA, USA, where he designed avionics systems for aerospace research projects. His current research interests include design of ultralow-power backscatter communication systems for biomedical applications.

**Alexandra Pike** received the B.A. degree in physics and French from Grinnell College, Grinnell, IA, USA, in 2008, the M.Litt. degree in Celtic studies from the University of Aberdeen, Aberdeen, Scotland, in 2010, and the MIT degree in secondary science from the University of Washington, Seattle, WA, USA, in 2012.

Since 2012, she has been a Physics Teacher with the Juanita High School, Kirkland, WA, USA, where she became a National Board Certified Teacher in 2017. From 2016 to 2017, she was an NSF Research Experience for Teachers (RET) Researcher with the University of Washington. Her current research interests include high school physics and engineering education and teacher professional development.

**Anissa Dadkhah** (S'18) received the B.S. degree in electrical engineering from the University of Washington in Seattle, WA, USA, where she is currently pursuing the M.S. degree in electrical engineering with the University of Washington.

Her current research interests include electromagnetics and embedded systems.

**Matthew S. Reynolds** (S'01–M'02–SM'10) received the S.B., M.Eng., and Ph.D. degrees from the Massachusetts Institute of Technology, Cambridge, MA, USA, in 1998, 1999, and 2003, respectively.

He is a Co-Founder of the RF identification (RFID) systems firm, ThingMagic, Inc., Cambridge, MA, USA, the demand-side energy conservation technology firm, Zensi, Playa Vista, CA, USA, the home sensing company, SNUPI Technologies, Inc., Seattle, WA, USA, and the millimeter-wave imaging firm, ThruWave LLC, Seattle, WA, USA. He is currently an Associate Professor of electrical engineering and computer science and engineering with the University of Washington, Seattle, WA, USA. His current research interests include the physics of sensors and actuators, RFID, microwave and millimeter-wave imaging, and sensor signal processing.